ACS APPLIED BIO MATERIALS

www.acsabm.org Article

Auranofin-Loaded Chitosan Nanoparticles Demonstrate Potency against Triple-Negative Breast Cancer

Maame Abena O. Afrifa, Jong H. Kim, Kathryn A. Pitton, Chibuzor Olelewe, Adedamola S. Arojojoye, Douglas R. Strachan, Mark A. Suckow, and Samuel G. Awuah*

Cite This: *ACS Appl. Bio Mater.* 2024, 7, 2012−2022 Read Online

ACCESS | Metrics & More | Article Recommendations | Supporting Information

ABSTRACT: Triple-negative breast cancer (TNBC) remains a clinical challenge due to molecular, metabolic, and genetic heterogeneity as well as the lack of validated drug targets. Thus, therapies or delivery paradigms are needed. Gold-derived compounds including the FDA-approved drug, auranofin have shown promise as effective anticancer agents against several tumors. To improve the solubility and bioavailability of auranofin, we hypothesized that the nanodelivery of auranofin using biodegradable chitosan modified polyethylene glycol (PEG) nanoparticles (NPs) will enhance anticancer activity against TNBC by comparing the best nanoformulation with the free drug. The selection of the nanoformulation was based on synthesis of various chitosan PEG copolymers via formaldehyde-mediated engraftment of PEG onto chitosan to form [chitosan-*g*-PEG] copolymer. Furthermore, altered physiochemical properties of the copolymer was based on the formaldehyde ratio towards nanoparticles (CP 1−4 NPs). Following the recruitment of PEG onto the chitosan polymer surface, we explored how this process influenced the stiffness of the nanoparticle using atomic force microscopy (AFM), a factor crucial for in vitro and in vivo studies. Our objective was to ensure the full functionality and inherent properties of chitosan as the parent polymer was maintained without allowing PEG to overshadow chitosan's unique cationic properties while improving solubility in neutral pH. Hence, CP 2 NP was chosen. To demonstrate the efficacy of CP 2 NP as a good delivery carrier for auranofin, we administered a dose of 3 mg/kg of auranofin, in contrast to free auranofin, which was given at 5 mg/kg. In vivo studies revealed the potency of encapsulated auranofin against TNBC cells with a severe necrotic effect following treatment superior to that of free auranofin. In conclusion, chitosan-*g*-PEG nanoparticles have the potential to be an excellent delivery system for auranofin, increasing its effectiveness and potentially reducing its clinical limitations.

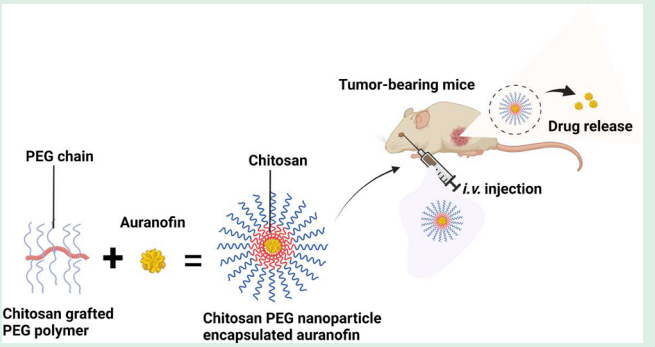

KEYWORDS: *auranofin, chitosan, PEG, nanoparticle, triple-negative breast cancer (TNBC), atomic force microscopy (AFM)*

INTRODUCTION

Nanoscale encapsulation and drug delivery of chemotherapeutic agents present viable opportunities that offset poor drug solubility, tissue biodistribution, circulation half-life, toxicity, and chemical instability liabilities for enhanced drug action.[1−3] Chitosan-derived nanoparticles, produced by copolymer grafting of hydrophilic polymers such as polyethylene glycol (PEG) unto cationic chitosan, enable the creation of biocompatible materials with tunable properties toward multifunctional nanodevices.[2,4] This offers an iterative platform for smart integration of targeting groups and therapeutics to improve selective drug accumulation, limit premature clearance, and unveil novel applications in theranostics, bioadhesion, wound healing, and stimulus-responsive polymer engineering. Chitosan-derived nanoparticles represent a well-established technology that has been applied in local and systemic delivery as well as therapeutic targeting. To achieve clinical approval of chitosan-based drug delivery, precision engineering of chitosan NPs is desperately needed.

Polymeric nanoparticles (NPs) play a crucial role in the efficient delivery of drugs to targeted areas, which increases bioavailability and limits side effects.[5−9] The selection of nanocarriers for auranofin relies on the physicochemical properties of the delivery system. Among the current nanodelivery systems, poly(lactic-*co*-glycolic acid) (PLGA) is a commonly used synthetic polymer with favorable attributes.[10] Chitosan, on the other hand, is a natural polymer that is well studied for many biomedical and pharmaceutical

Received: February 7, 2024
Revised: February 17, 2024
Accepted: February 21, 2024
Published: March 7, 2024

https://doi.org/10.1021/acsabm.4c00184
ACS Appl. Bio Mater. 2024, 7, 2012−2022

applications due to its biodegradable, biocompatible, and nontoxic qualities.[11] The use of chitosan microspheres and nanoparticles for drug delivery was first documented in the late 1990s.[11−14] The multifunctionality of chitosan chemically is centered on the ability to become a polycationic charged molecule at acidic pH because of the protonation of D-glucosamine, polymeric structure, and adjustable molecular weight.[3,11,15,16] Chemical and biological properties of chitosan are obtained by the deacetylation of chitin, molecular weight, and types of surface modifications.[11] Comparing PLGA to chitosan, a significant drawback of PLGA is its hydrophobic nature, which triggers the activation of the reticuloendothelial system (RES), and RES is responsible for eliminating nanosystems through opsonization.[17] The surface interface plays a crucial role in the nanocarrier's elimination process, and chitosan possesses appealing traits such as cationic properties that render it soluble in acidic environments like the gastrointestinal region.[18−20] Studies have indicated the coating of lower-molecular-weight chitosan onto PLGA surfaces to serve as a hydrophilic coating, making chitosan an ideal delivery system for auranofin.[17] In this study, PEG was coated on the surface of chitosan to enhance therapeutic indices and solubility under neutral pH, considering that chitosan is soluble under acidic conditions. Chitosan-*g*-PEG copolymers were created in the presence of formaldehyde to enhance the solubility and biocompatibility of chitosan.[21−25] However, investigations to resolve the prevailing bottlenecks surrounding chitosan NP engineering and to maximize their physicochemical properties for enhanced drug delivery remain underexplored.

Metallodrugs such as platinum-based agents have been employed to treat variety of cancers.[26] Despite the positive effects of these agents, drawbacks such as resistance and toxic side effects can lead to tumor recurrence and death.[27,28] Gold-based complexes have become popular in recent years due to their unique anticancer activity, which differs from cisplatin's mode of action.[29] Auranofin (AUF) is a gold-containing oral drug approved by the FDA for treating rheumatoid arthritis since 1985.[30−34] Auranofin alters the redox systems that cancer cells use to control high levels of reactive oxygen species, which then leads to cancer death.[30,35−40] It has been repurposed as a powerful anticancer drug and is currently undergoing clinical trials for the treatment of chronic lymphocytic leukemia, ovarian cancer, and lung cancer.[30,31,35−37,41] Triple-negative breast cancer (TNBC) is a type of breast cancer that lacks expression of estrogen, progesterone, and human epidermal growth factor receptor 2 expression.[42−44] TNBCs make up about 15−20% of the total of all breast cancers, and in 2021, 281,550 new cases and 43,600 deaths of TNBC were recorded in the United States.[45−48] It accounts for most breast cancer-related deaths as there are limited treatments options for this patient population.[45,47,49] Auranofin has the potential to be an effective anticancer agent but is known to be insoluble in neutral pH and has been demonstrated to cause significant adverse effects.[50,51] The effectiveness of auranofin as a potential anticancer drug for TNBC could be increased by nanodelivery to these cancer cells. Overall, design parameters for chitosan-based delivery of metallodrugs, including auranofin, will improve the effectiveness and safety by controlling the dosage, duration of effect, and tumor-specific release.

Whereas various nanoparticle designs including surface coatings and different nanoparticle sizes and shapes have been studied, the mechanical properties elucidating how various designs and coatings affect deformability and flexibility have been underexplored. The size and surface effects of the nanoparticle allow varying mechanical properties, and elucidating this property is key in the selection of nanoparticles for in vitro and in vivo novel applications.[52−54] In this study, we demonstrate that physicochemical properties and stiffness of chitosan NPs can be tuned by optimizing PEG (PEG8000) content to enable the encapsulation of the FDA-approved metallodrug auranofin for intracellular delivery. We show that chitosan NPs demonstrate an increased stability of intact auranofin and overall speciation. Interestingly, chitosan NPs can deliver auranofin cargo into cells toward the induction of apoptosis in TNBC cells as well as inhibit TNBC tumor growth in the aggressive, metastatic 4T1 mouse model at low doses with no adverse effect on body weight in vivo, thus extending the breadth of prior observations of chitosan as a multifunctional drug delivery system.

EXPERIMENTAL SECTION

Materials. Medium-molecular-weight chitosan (44877-50G from Sigma-Aldrich, molecular weight 262 kDa, degree of deacetylation 76.9%) and polyethylene glycol (PEG) (molecular weight 8000 Da, 043443.36) were purchased from Aldrich chemical Co. Inc. (USA). Auranofin was bought from (VWR). DiD dye (1,1′-dioctadecyl-3,3,3′,3′-tetramethylindodicarbocyanine,4-chlorobenzenesulfonate) salt was purchased from Thermo Fisher Scientific. Formaldehyde, DCM, acetone, acetic acid, and PBS were all purchased from commercial vendors.

Methods. *Synthesis of Chitosan Grafted PEG Copolymers.* Chitosan grafted PEG was synthesized using the formaldehyde linkage method.[55] A 100 mg portion of chitosan was poured in a 150 mL round-bottomed flask. Five milliliters of formic acid was added to chitosan in the flask and allowed to stir for 15 min. After 15 min, 45 mL of DMSO was added to the dissolved chitosan mixture, and 1.2 g of PEG of molecular weight 8000 Da was weighed, added to the mixture in the flask, and left to stir for 15 min. After 15 min, 0.5, 5, 10, or 20 mL of formaldehyde solution depicting the formation of copolymer 1 (CP1), copolymer 2 (CP2), copolymer 3 (CP3), and copolymer 4 (CP4), respectively, was added to the polymer mixture in the flask and allowed to stir for 12 h. After 12 h, the resulting mixture was then added dropwise to a cold acetone solution stored in a −20 °C freezer for 30 min. A white precipitate was seen and dialyzed in DI water using a 10 kDa MWCO centrifuge tube to remove unreacted PEG. The solution in the inner chamber of the filter tube was then washed with DI water by centrifugation at 6000 rpm for 20 min. The resulting gel was freeze-dried overnight to form a dry copolymer. The dried polymer was stored at room temperature for further use.

Chitosan Grafted PEG Copolymer Characterization. The copolymers were characterized using an NMR spectrometer (Bruker). For consistency across the copolymers, ^{1}H NMR spectra of the copolymer were recorded in D_2O and 2% acetic acid at 25 °C, and the concentration of the polymer was 4 mg mL^{-1}

Preparation of Chitosan PEG Nanoparticles. Auranofin-loaded nanoparticles (NPs) were synthesized using the ionic gelation method with slight modifications. Briefly, 50 mg of chitosan grafted PEG was dissolved in 2 mL of 2% acetic acid and stirred for 15 min. After 15 min, auranofin was dissolved in a mixture of 10 mL of acetone and DCM to make up a concentration of 500 or 10 μM. When encapsulated with fluorescent dye (DiD) instead of auranofin to visualize the release, 2 mg of the dye was dissolved in same solvent. The mixture was sonicated to ensure that auranofin/DiD was completely dissolved and added to the copolymer mixture. Sodium sulfate (1 mg/mL) as the ionic linker in this case was added dropwise at 0.2 mL/min to the copolymer solution, stirred for 1 h at 500 rpm, and stirred for another hour at 300 rpm. The organic solvent via

https://doi.org/10.1021/acsabm.4c00184
ACS Appl. Bio Mater. 2024, 7, 2012−2022

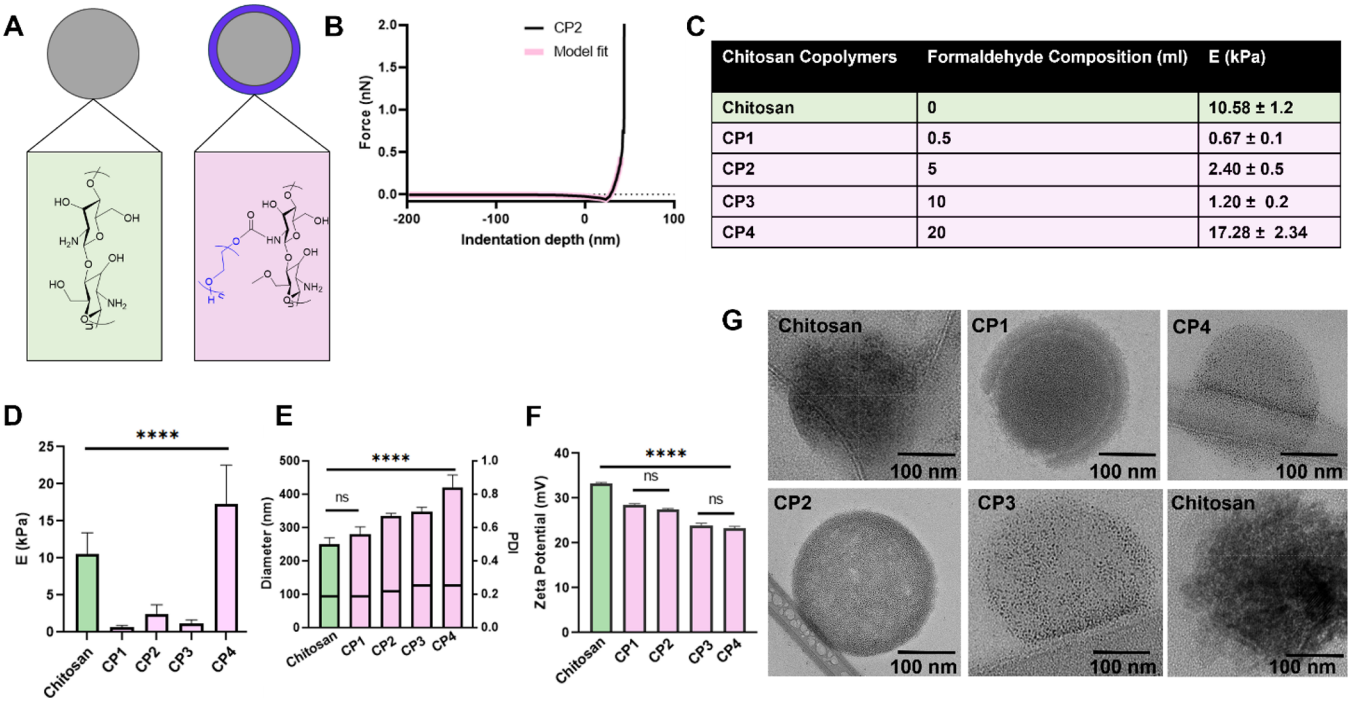

Chitosan Copolymers	Formaldehyde Composition (ml)	E (kPa)
Chitosan	0	10.58 ± 1.2
CP1	0.5	0.67 ± 0.1
CP2	5	2.40 ± 0.5
CP3	10	1.20 ± 0.2
CP4	20	17.28 ± 2.34

Figure 1. Physiochemical characterization of chitosan grafted PEG nanoparticle. (A) A schematic drawing of the chitosan nanoparticle and a double layered chitosan modified PEG. (B) Force curve demonstrating the model fit employed to generate the elastic moduli of the nanoparticles after indentation. (C) Modified chitosan nanoparticle is formulated with 8000 Da PEG with different compositions of formaldehyde. The table depicts the various compositions of the copolymers synthesized into the various nanoparticles and various stiffness values, where CP 1, CP 2, CP 3, and CP 4 mean copolymer 1, copolymer 2, copolymer 3, and copolymer 4 respectively. (D) The AFM measurements demonstrate the elastic modulus E ($P < 0.0001$) difference between the nanoparticles and force curve showing the various distributions. The data show that the stiffness decreases as more PEG is recruited unto the chitosan to form a nanoparticle due to the fluffy coating of the PEG changing the mechanical properties of chitosan. An increase in stiffness is seen when oversaturation occurs after more PEG components are recruited on the chitosan surface. (E) Size and zeta potential were measured using an Anton Paar particle size analyzer. No significant difference in the polydispersity was seen between the copolymer NPs. (F) The zeta potential was also measured using the Anton Paar particle size analyzer. (G) TEM images of chitosan and copolymers indicate a bare spherical structure of the pristine in contrast the copolymer NPs showing a fluffy coat surrounding the chitosan as the core due to the presence of the hydrophilic component PEG.

rotary evaporation at room temperature (RT) was removed. Nanoparticles acquired for copolymers 1, 2, 3, and 4 were collected, sonicated for 10 min, and centrifuged at 6000 rpm for 30 min at 18 °C using a 50 kDa MWCO centrifugal filter. The nanoparticles were washed three times with 2 mL of PBS to remove unencapsulated auranofin or dye. The washed NPs were stored in a 4 °C freezer for further use.

Encapsulation Method. The stock solutions 500 and 10 μM of auranofin were prepared using a ratio between DCM and acetone based on an already reported work. The known concentrations of the gold drug were each added to the nanoparticle formation and left to stir for 2 h. After 2 h, the nanoparticle solution was rotovapped to remove organic solvents and washed thoroughly through centrifugation to remove unencapsulated gold drug. One hundred microliters of the washed nanoparticle was introduced to 1000 μL of 2 M HCl solution. The HCl mixture was then incubated for 3 h, and GFAAS analysis was done to determine the encapsulated gold. The equation below was used to determine the efficiency and loading capacity after GF-AAS analysis.

$$\text{Encapsulation efficiency(EE)} = \frac{\text{final concentration of auranofin}}{\text{initial concentration of auranofin}} \times 100\%$$

$$\text{Loading capacity(LC)} = \frac{\text{weight of auranofin encapsulated}}{\text{weight of nanoparticle}} \times 100\%$$

Chitosan PEG Nanoparticle Characterization. The morphology of the chitosan NPs was determined using transmission electron microscopy (TEM) (Talos F200X). NP solution of 40 μL was added to 2 mL of distilled water. A drop of the diluted NP suspension was deposited on a copper grid, air-dried for 24 h, and observed under the microscope. The size and zeta potential of the chitosan nanoparticles were determined using a Litesizer Anton-Paar particle size analyzer at 25 °C. The nanoparticle was diluted with 1 mL of ultrapure water for the analyses.

Atomic Force Microscopy. Sample preparation for the AFM measurements was performed in a clean environment. Samples were diluted in Milli-Q H_2O at a 1:1000 ratio of sample/Milli-Q H_2O, and a 10 μL suspension of each nanoparticle sample was drop cast onto a clean SiO_2 surface located on an ~10 mm square Si substrate for AFM imaging. The drop was allowed to evaporate in air, and the suspension solids bound to each surface. The residual solids formed random arrangements of blotches and circles of various coagulations and heights.

Atomic force microscopy (AFM) imaging was performed using an Asylum Research MFP-3D instrument in AC mode and contact mode. Images were initially collected using the AC mode to find areas of interest. The AFM was then switched to contact mode, and the InVOLs and spring constant were calibrated on the SiO_2 surface for hardness. For force curve analysis, 15 nanoparticles for each sample were identified and targeted. The speed of the cantilever approach/retraction was set at 450 nm/s, and the retraction of the probe was initiated upon reaching the maximum force of ~10 nN with an indentation depth of up to 20 nm for all types of nanoparticles. A single force curve was collected for each selected nanoparticle. Images

https://doi.org/10.1021/acsabm.4c00184
ACS Appl. Bio Mater. 2024, 7, 2012−2022

and force curves were collected using Tap300AI-G, a tapping mode AFM probe with a silicon overall coating and alumina reflective coating (force constant 40 N/m, resonant frequency 300 kHz, and tip thickness of 4 μm) (Budgetsensors). All images were collected and processed (flattened and Hertz-fit) by using the IgorPro software.

In Vitro Release Assay. The release rate of auranofin encapsulated in the nanoparticle was determined at different time points (4, 8, 12, and 24 h) and pH 4.0 simulating an acidic medium such as the pH of the stomach and 7.4 simulating physiological pH. At each time point, 2 mL of the nanoparticle solution was dispensed in the inner membrane of the 15 mL dialysis tube (Sigma dialysis tubes Mw cutoff 3 kDa). Three milliliters of PBS was added to the 2 mL of nanoparticle solution already in the tube and placed in a shaker at 100 rpm at a temperature of 37 °C. At different time points (4, 8, 12, and 24 h), 0.5 mL of the supernatant was taken out and replaced with the same volume taken out. The collected solution of the released auranofin at each time point was then analyzed by using HPLC.

In Vivo Studies. Six week old female BALB/cJ 4T1 mice were used for the studies. The mice were randomly divided into three groups, i.e., the control group, unencapsulated auranofin group, and encapsulated auranofin group, with five mice (n = 5) in each group. The mice were left for 1 week to acclimatize before injecting 500,000 4T1 cells subcutaneously on their flanks. After 3 days of implantation, the mice were injected with 5 mg/kg of unencapsulated auranofin and 3 mg/kg encapsulated auranofin with DMSO (1%) and PBS solution for the control group. Retroorbital Injections were made three times per week. Before every injection, tumor sizes were measured using calipers, and body weights of the mice were measured after injection. Mice were euthanized on the 16th day, and various tissues (spleen, kidney, heart, lungs, and liver) were removed for H&E staining.

Statistical Analysis. The statistical analysis was conducted with the Student t test and one-way ANOVA, and all data were presented as the mean ± SEM. All data from the article were made using ORIGIN PRO and GraphPad Prism 6.0 (GraphPad Software).

RESULTS AND DISCUSSION

Pegylation Modulates C-NP Effective Elastic Moduli and Outer Layer Stiffness. Despite the prevalence of chitosan NPs (C-NPs), their utility for metallodrug delivery is uncommon, and a detailed physicochemical characterization remains underexplored. Chitosan NPs (C-NPs) display higher effective elastic moduli in comparison to copolymer NPs (CP 1−3 NPs) except CP4 NP. Before the nanoparticle synthesis, the copolymers CP 1−4 were characterized by NMR and Fourier-transform infrared spectroscopy (Figures S1−S3). High-molecular-weight chitosan is insoluble in neutral aqueous solvent but is soluble at low pH, and to address this bottleneck, PEG grafted onto the amine groups of the chitosan backbone improved solubility with direct correlation to PEG recruitment, as evidenced by a quantitative solubility test (Figure S4). The degree of substitution (DS) values for the copolymers CP 1−4 are 23, 28, 39 and 49%, respectively. Given that PEG is FDA-approved and has been used to improve the solubility, bioavailability, and circulation half-life of nanoparticles, as well as the impact the rheological properties of chitosan hydrogels,[56] we hypothesized that PEG is capable of modulating physicochemical properties of chitosan NPs and would be useful for maximum delivery of a broad array of cargo including metallodrugs. For consistency, we used PEG8000 as the PEG agent of choice. We subsequently formulated the nanoparticle via the ionic gelation method using sodium sulfate as the ionic linker for both the C-NP and CP 1−4 NP classes of nanoparticles.

The mechanical classification of individual NPs was derived, and using effective stiffness as a critical parameter, the elastic moduli E for C-NP and CP 1, 2, 3, and 4 NPs were computed by atomic force microscope-enabled indentation on hydrated NPs. The representative force displacement feedback is summarized in Figure 1B, and the quantifiable elastic moduli were extrapolated from n = 15 measurements per composition using the Hertz model by which the adhesion component of the nanoparticle seen was negligible and did not affect the calculation of the elastic moduli values (Figure S5−S14).

We found that variations in the relative magnitudes of individual NPs were significant and were a function of PEG coating, composition, and architecture of NPs. C-NPs exhibited effective E of 10.58 ± 1.2 kPa, whereas CP-NPs display effective E of 0.67 ± 0.1, 2.40 ± 0.5, 1.20 ± 0.2, and 17.28 ± 2.34 kPa, respectively, as seen in Figure 1C. As PEG composition increases, we observe a significantly low elastic property for CP 1−3 NPs with an increase seen in CP4 NP, suggesting that core chitosan composition dictates NP stiffness as seen in Figure 1D. The increase in elastic property seen in CP4 NP may be associated with oversaturation of PEG polymer unto chitosan, which imposes a change in the stiffness of the nanoparticle. Changes in the PEG coating content did not significantly alter the particle diameter when the CP-NP formulations were measured by dynamic light scattering (DLS) and showed good stability under different temperature conditions (Figure S15). C-NPs were 249 ± 11.8 nm, and CP 1−4 NPs were 280 ± 13.1, 334 ± 4.9, 348 ± 7.4, and 421 ± 21.3 nm, respectively (Figure 1E). Additionally, zeta potential measurements did not show significant differences based on PEG content, where C-NPs were +33.23 ± 0.27 and CP 1−4 NPs were +28.51 ± 0.21, +27.50 ± 0.23, +23.90 ± 0.50, and +23.30 ± 0.40 mV, respectively, as shown in Figure 1F and Figure S16. The slight decrease in the potential for CP -NPs compared to C-NP might be due to the presence of in the PEG content, which may result from the neutral PEG covering the surface of the nanoparticle.

The effect of PEG content on NP architecture was examined by transmission electron microscopy (TEM) as depicted by the images of our NPs in Figure 1G. A spherical nanoparticle is seen, and this observed architecture of the nanoparticles is likely due to the negative ions of sodium sulfate interacting with the positive ions of the chitosan and incorporation of neutral PEG. This observation is consistent with similar reports of other derivatives of chitosan/PEG and chitosan/PEO−PPO nanoparticles by Zhang et al. and Calvo et al., respectively.[12,21] Additionally, the results demonstrate significant structural differences in the chitosan core structure and the outer layer morphology. C-NPs have an undefined outer structure with no surrounding layer. In contrast, CP-NPs formulated with PEG8000 have a defined, circular, and fluffy outer layer, indicative of a PEG coating of the chitosan core. It is possible that the PEG end groups are directed to the surface, primarily due to its hydrophilic character.[55,57,58] The fluffy coating is noted to become dense as the PEG content increases per the copolymers. CP1 NP shows a formation of PEG layer with a varying degrees of 70−95% PEG coating demonstrating an incomplete circular coating, and this observation might be due to the low amount of PEG grafting on the chitosan. CP2 NP shows complete formation of the PEG layer, with CP3 and CP4 NPs showing no difference between the chitosan core and the coating, and this is likely due to the presence of excess PEG formulation embedded together with the core. Based on the morphological difference observed in the TEM image between the copolymer nanoparticles CP 1−4, CP2 NPs is the nanoparticle of choice. CP2 showcased a perfectly spherical

https://doi.org/10.1021/acsabm.4c00184
ACS Appl. Bio Mater. 2024, 7, 2012−2022

nanoparticle structure, indicating 100% coating of the PEG around the chitosan core. We aimed to retain the full functionality and inherent properties of chitosan as the parent polymer without allowing PEG to overshadow its unique cationic properties. This is evident in Figure 1F, illustrating a slight decrease in the cationic charge property for CP3 and CP4. Moreover, Figure 1G highlights the morphological similarities between CP3, CP4, and the embedding of PEG in the core, causing negligible difference between the chitosan and PEG, which in this case has the potential to alter the unique properties of both polymers. CP1, on the other hand, exhibited varying degrees of incomplete coating of PEG, ranging from 70 to 95%, rendering it unreliable for fully leveraging the properties of the copolymer.

Formulation and Characterization of Auranofin-loaded CP-NPs. Based on the characterization data for CP-NPs, we prioritized CP2 NP also due to its desirable mechanical rigidity for drug delivery applications. Of note, the optimal mechanical strength of a nanoparticle is particularly attractive to ensure that the nanoparticles circumvent elimination or premature cargo release.[52] Additionally, CP2 avoids the excessive stiffness of the nanoparticle. This is crucial as most chitosan nanoparticles rely on protonation of the amine groups, degradation properties, and liquid infiltration to trigger swelling to facilitate cargo release. Therefore, we used CP 2 polymer nanoparticles to encapsulate auranofin for delivery via ionic gelation.

As shown in Figure 2A, the characteristic morphology and size of both empty and auranofin-loaded CP2 NPs as depicted by TEM are spherical, with a PEG coated outer layer. Further, the dark fields observed in gold-loaded CP2 NPs could be attributed to the presence of gold from the auranofin cargo and was confirmed with energy dispersive spectroscopy (EDS) (Figure 2A right image). The changes seen in the loading positions of the gold drug might be due to the preparation method of the TEM and the drying mechanism of the nanoparticle on the grids, which caused an increase in high surface energy and surface tension specifically in the drying process. Using a critical point dryer in the future is likely to reduce the surface tension of the biological material and ensure the centered position of the gold drug. The particle size was determined by DLS using an Anton Paar particle size analyzer as shown in Figure 2B. The hydrodynamic nanoparticle mean size was 334 ± 4.9 nm. We note that the varying sizes of chitosan-*g*-PEG nanoparticles reported in the literature thus far might be due to different preparation methods and conditions, such as varying the polymer-to-ionic linker ratio, varied PEG length, and different PEG recruitment on the amino groups of chitosan. The observed zeta potential was +28.3 ± 0.14 mV as shown in Figure 2C.

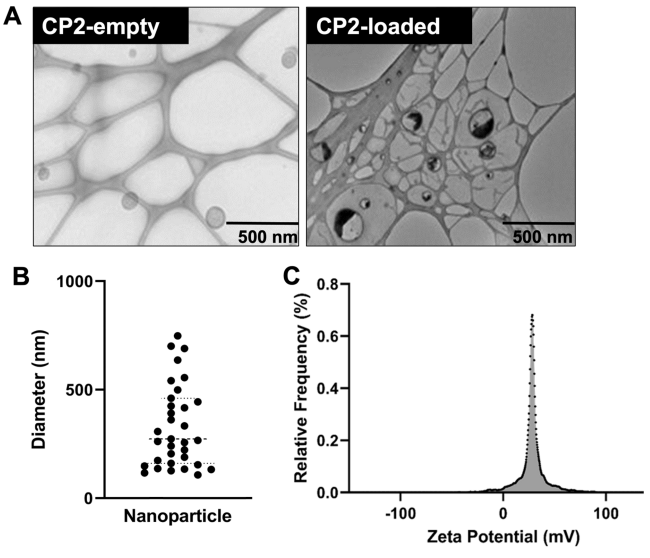

Figure 2. Synthesis and characterization of the chitosan-*g*-PEG nanoparticle (CP2). (A) TEM photograph of the nanoparticle. Empty chitosan-*g*-PEG nanoparticles (left) and chitosan-*g*-PEG nanoparticles loaded with auranofin (right) (chitosan-*g*-PEG/Na_2SO_4 = 2:1). The presence of the gold drug auranofin encapsulated in the core of the nanoparticle may be due to hydrophobic interactions between the chitosan at the core and auranofin. (B) Size distribution spectrum of auranofin loaded nanoparticles using an Anton Paar particle size analyzer with the average size reported as mean ± SEM with dashed lines as the mean and dotted line as SEM. (C) Zeta potential of auranofin loaded nanoparticles.

Kinetic Release Profiles of Auranofin-Loaded CP-NP. To fully characterize kinetic release profiles, it is important to develop a robust assay methodology to quantify released cargo. We utilized a rigorous LC−MS assay method to measure auranofin with concomitant speciation of auranofin. The experiment was run at the same time point for all of the copolymer nanoparticles. Using a sensitive single ion monitoring ESI-MS method coupled to the LC, we assayed auranofin. Under the ESI positive mode conditions utilized, two significant peaks of 663 and 993 *m*/*z* were observed, which are attributed to the auranofin-methyl fragment [M-15] and dinuclear Au(I) bis-triethylphosphine substituted derivatives, respectively (Figure 3A,B).

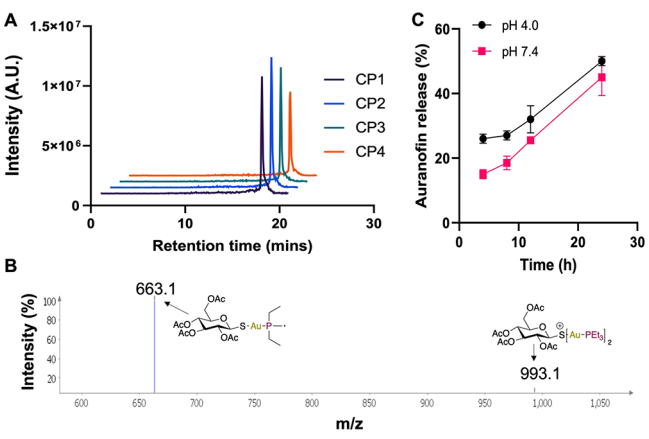

Figure 3. Speciation of auranofin using liquid chromatography−mass spectrometry (LC−MS) and kinetic release profiles. (A) HPLC chromatogram of auranofin after the nanoparticle is digested to release the encapsulated gold drug. No significant difference in auranofin retention rate was seen between the copolymer nanoparticles ($P > 0.05$). (B) Auranofin structure seen in single-ion monitoring (SIM) LC−MS after the different types of nanoparticles (CP1, CP2, CP3, and CP4) were digested to release the encapsulated auranofin. Two peaks consistent with auranofin were seen, with 663 being more prominent than the 993 peak. (C) The release of CP2 nanoparticle at different time points (4, 8, 12, and 24 h) and different pH was analyzed. At pH 4.0, a significant release of the gold drug was seen relative to pH 7.4, and this may be due to the protonation of the positive charge on the surface of the chitosan that causes more release of the drug than pH 7.4.

https://doi.org/10.1021/acsabm.4c00184
ACS Appl. Bio Mater. 2024, 7, 2012−2022

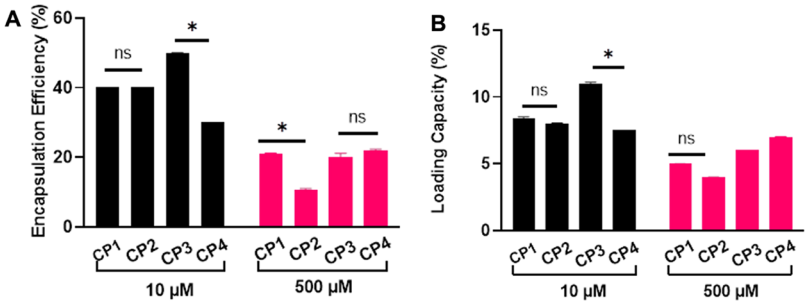

Figure 4. Encapsulation efficiency and loading capacity of auranofin loaded NP gold quantification by using GF-AAS. (A) Encapsulation efficiency (%). Two different nanoparticle stock concentrations were used at 10 and 500 μM. The encapsulation efficiency was seen to be higher in 10 μM compared to 500 μM, which might be due to the oversaturation of auranofin in 500 μM. Also, CP3 NP showed the highest efficiency with no difference between CP1 NP and CP2 NP and a lower concentration observed in CP4 NP at 10 μM and slight changes at 500 μM. (B) Loading capacity (%). CP3 NP had the highest loading capacity with not much difference between CP1 NP, CP2 NP, and CP4 NP (* represents $P < 0.05$).

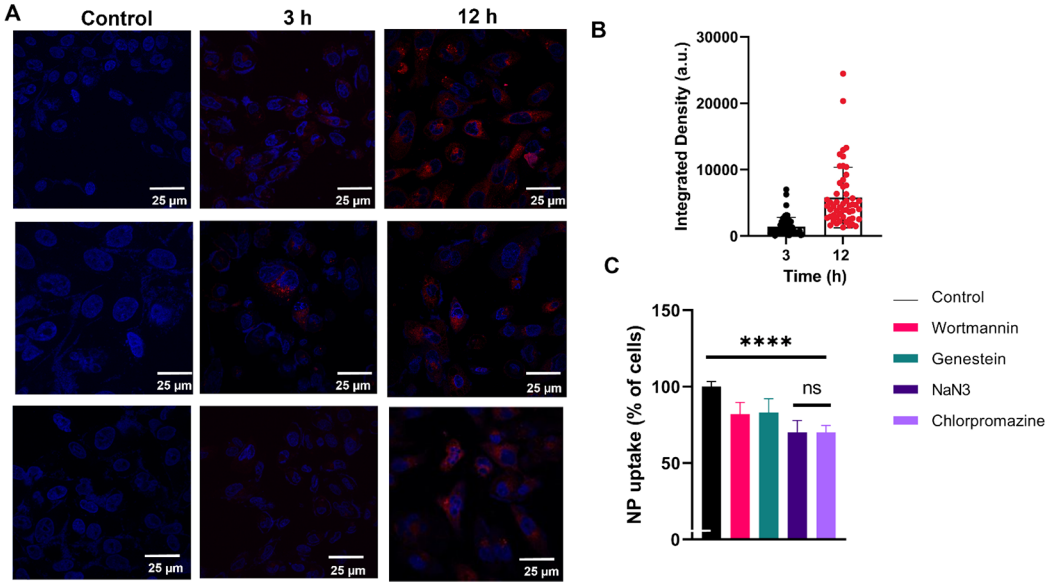

Figure 5. In vitro studies of the MDA-MB-231 TNBC cell line. (A) Confocal image showing cellular uptake and release mechanism, DAPI (blue), and encapsulated DiD dye (red). DiD dye was encapsulated into CP2 NP nanoparticle to determine the mode of release of the nanoparticle at time points 3 and 12 h. More dye was released after 12 h with a relatively low release at 3 h. Scale bar: 25 μm, magnification: 20× (experimental detail can be found in the SI). (B) Fluorescence quantification. The intensity of dye released was measured at time points 3 and 12 h using the ImageJ software with 12 h showing the highest intensity value. (C) Cellular uptake mechanism (**** represents $P < 0.05$). The mechanism of cellular uptake was determined by using four different pathway inhibitors: sodium azide (NaN_3) known to inhibit mitochondrial oxidative phosphorylation, chlorpromazine known to inhibit clathrin-dependent endocytosis, wortmannin known for micropinocytosis inhibition, and genestein for clathrin-independent endocytosis. The results showed the probability of nanoparticles being taken up by endocytosis.

We evaluated the rate of cargo release from the auranofin-loaded CP2 NPs to fully characterize the kinetic behavior of these nanoparticles. The rate of release of the auranofin was determined using a 50 kDa MWCO centrifugal filter with the nanoparticle solution embedded in the inner core of the filter and placed in a shaker at 100 rpm and 37 °C. At time points 4, 8, 12, and 24 h, the auranofin release was measured by LC−ESI-MS at each time point of release as described above. Quantification was achieved by using a standard curve in the range of 1, 10, 100, and 1000 ppm. The nanoparticle release was steady and continuous with a pronounced release by 24 h. Figure 3C shows the slow release observed with an indication that the concentration of auranofin is expected to increase after 24 h, as potential nanoparticle swelling occurs. The initial release of auranofin was quite fast with about 18 and 22% at pH 7.4 and 4.0, respectively, during the first 4 h and constant release rate between 8 and 12 h at both pH 7.4 and 4.0. This could be because chitosan with a molecular weight ranging between 190 and 300 kDa has a high positive charge that forms a dense network that slows the release of auranofin. Longer chain segments have been known to impact both diffusion of cargo and degradation of nanoparticle, leading to the release of entrapped cargo.[21] As a result, we posit that the release of auranofin at the allotted time points is likely due to simple diffusion rather than degradation of the whole nanoparticle.

Encapsulation Efficiency (EE) and Loading Capacity (LC) of Encapsulated Auranofin. To determine the encapsulation efficiency and loading capacity of CP-NPs, we made two different stock solutions of auranofin at a lower and higher concentration of 10 and 500 μM, respectively. Following our established protocol for cargo-loaded chitosan nanoparticle synthesis as described above, auranofin-loaded CP1−4 NPs were synthesized and characterized. With drug-loaded CP-NPs in hand, 100 μL of the NP solution was added

https://doi.org/10.1021/acsabm.4c00184
ACS Appl. Bio Mater. 2024, 7, 2012−2022

to 1 mL of 2 M HCl and incubated for 3 h. Following digestion, auranofin in the solution was assessed by using graphite furnace atomic absorption spectroscopy (GFAAS), which specifically determined the gold content found in the digested nanoparticle solution. The encapsulation efficiency and loading capacity were seen to be higher in 10 μM auranofin feedstock solution compared to 500 μM (Figure 4). The 10 μM stock solution had an encapsulation efficiency of 40% for CP1 NP and CP2 NP, 50% for CP3 NP, and 24% for CP4 NP as seen in Figure 4A. The decrease in EE seen in CP4 NP may be due to the high PEG content on the surface of chitosan, which increases the hydrophilicity of the nanoparticle and consequently limits the interaction of the core chitosan and auranofin for efficient encapsulation. The EE for CP1-CP4 NP in the 500 μM stock solution was observed to be 20, 10, 20, and 20%, respectively (Figure 4A). The drastic decrease in EE percentage observed at 500 μM relative to 10 μM might be due to cargo oversaturation. CP3 NP had the highest loading capacity with not much difference between CP1 NP, CP2 NP, and CP4 NP. Therefore, the design and composition of the nanoparticle play a role in both the encapsulation efficiency and loading capacity.

Cellular Response to Cargo-Loaded CP2 NPs. To see the mechanism of release of cargoes introduced in the MDA-MB 231 cancer cell line, the NPs were used to encapsulate DiD dye (red dye). The DNA of the cells was stained with DAPI (blue dye) before introducing the encapsulated dye to the cells. The NP encapsulated dye was incubated for 3 and 12 h, and the image seen in Figure 5A elucidates row 1 as control and rows 2 and 3 as time-based release of DiD dye. The release of the DiD dye was observed at different regions of the glass-bottomed dish, and more DiD dye (red) was seen to be released after 12 h compared to 3 h. This demonstrates that the cells were able to take up the nanoparticle regardless of the size reported in this study. The quantification of the fluorescence DiD dye released at each time point was analyzed using ImageJ, and the 12 h time points demonstrated an increase in intensity depicting more dye released relative to 3 h in Figure 5B.

The mechanism of NP uptake by TNBC cells was assessed to determine how the NPs are being taken up by the cells. For the studies, MDA-MB-231 cells were treated with sodium azide (NaN_3) known to inhibit mitochondrial oxidative phosphorylation, chlorpromazine known to inhibit clathrin-dependent endocytosis, wortmannin known for micropinocytosis inhibition, and genestein for clathrin-independent endocytosis with 1 μM of encapsulated auranofin for 24 h. The results in Figure 5C revealed minor inhibition of wortmannin and genestein inhibitor pathways whereas NaN_3 and chlorpromazine inhibitor pathways significantly ($p < 0.05$) reduced the uptake of the NPs by the cells. This is an indication that the nanoparticles are probably being taken up by endocytosis consistent with reported studies.[59,60]

The toxicity of auranofin loaded NPs and free auranofin was evaluated by an MTT assay, and the results are shown Figure 6A. The results revealed that both the encapsulated form and free auranofin were cytotoxic to triple-negative breast cancer cells, with IC_{50} values of 2.57 ± 0.32 μM and 2.39 ± 0.21 μM for auranofin-loaded NPs and free auranofin, respectively.

We explored the mechanism of cell death by auranofin-loaded NPs via annexin V−propidium iodide apoptosis assay by dual-colored flow cytometry analysis based on the established premise that free auranofin induces apoptosis as a mechanism of cell death (Figure S17).[61] We observed the induction of apoptosis by auranofin-loaded NPs in a concentration-dependent manner in Figure 6B. We performed the apoptosis assay at concentrations of 5 and 10 μM because 5 μM is twice the IC_{50} and 10 μM is quadruple that, demonstrating a more cytotoxic effect using higher concentration. These results together show that the encapsulated form of auranofin could effectively inhibit cell proliferation by inducing apoptosis consistent with free auranofin.

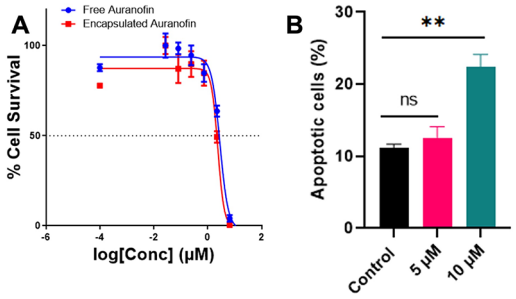

Figure 6. Cellular response to auranofin-loaded NPs. (A) Cell viability studies on TNBC cells. The viability of cells treated with auranofin and auranofin-NP was measured using the 3-(4,5-dimethylthiazol-2-yl)-2,5-diphenyltetrazolium bromide (MTT) assay. The IC_{50} value of auranofin was 2.39 ± 0.21 μM and that of auranofin-NP was 2.57 ± 0.32 μM, demonstrating no significant difference between both conditions but a cytotoxic effect seen from both on the cells. (B) Apoptosis studies of auranofin-NP (** represents $P < 0.001$). Auranofin is known to induce tumor cell death by inhibiting thioredoxin. Previous studies demonstrated apoptosis as the mode of cell death, and the concentration of encapsulated auranofin was varied at 5 and 10 μM. More cell death was seen in the 10 μM concentration at late apoptosis than the 5 μM concentration.

Encapsulated Auranofin Inhibits In Vivo TNBC Tumor Progression. We examined the therapeutic indices of encapsulated auranofin in TNBC tumor-bearing mice and benchmarked against auranofin seen in Figure 7. In vivo studies were conducted using a syngeneic 4T1 tumor mouse model in an immunocompetent background. As shown in Figure 7A, mice were treated with vehicle control (i.e., phosphate-buffered saline), free auranofin, or encapsulated auranofin, which was administered via retroorbital injection at a dose of 5 mg/kg of auranofin or 3 mg/kg of encapsulated auranofin at 6 doses 3 times a week. The treatment regimen was well-tolerated, with a remarkable tumor reduction seen in free auranofin and encapsulated auranofin even at relatively lower doses. The mean ± SEM tumor volumes for vehicle control, free auranofin, and auranofin-NP groups were 575.3 ± 102.4, 50.3 ± 6.2, and 68.2 ± 7.8 mm^3, respectively, as shown in Figure 7B with no statistical difference between the free auranofin and auranofin encapsulated nanoparticle. The body weight (mean ± SEM) values for vehicle, auranofin, and auranofin-NP were 19.46 ± 0.09, 18.03 ± 0.1, and 19.44 ± 0.1, respectively (Figure 7C). The body weight for the control and auranofin-NP group showed no significant difference, but a significant difference was seen between the control and auranofin-NP vs free auranofin group with $p < 0.0001$. Biodistribution studies performed using GF-AAS demonstrate a slight difference in gold accumulation in groups treated with auranofin-NP relative to free auranofin, proving the selectivity of chitosan NPs to tumor cells relative to free auranofin. More gold accumulation was seen in the kidney of free auranofin groups compared to auranofin-NP (Figure 7D), demonstrating

https://doi.org/10.1021/acsabm.4c00184
ACS Appl. Bio Mater. 2024, 7, 2012−2022

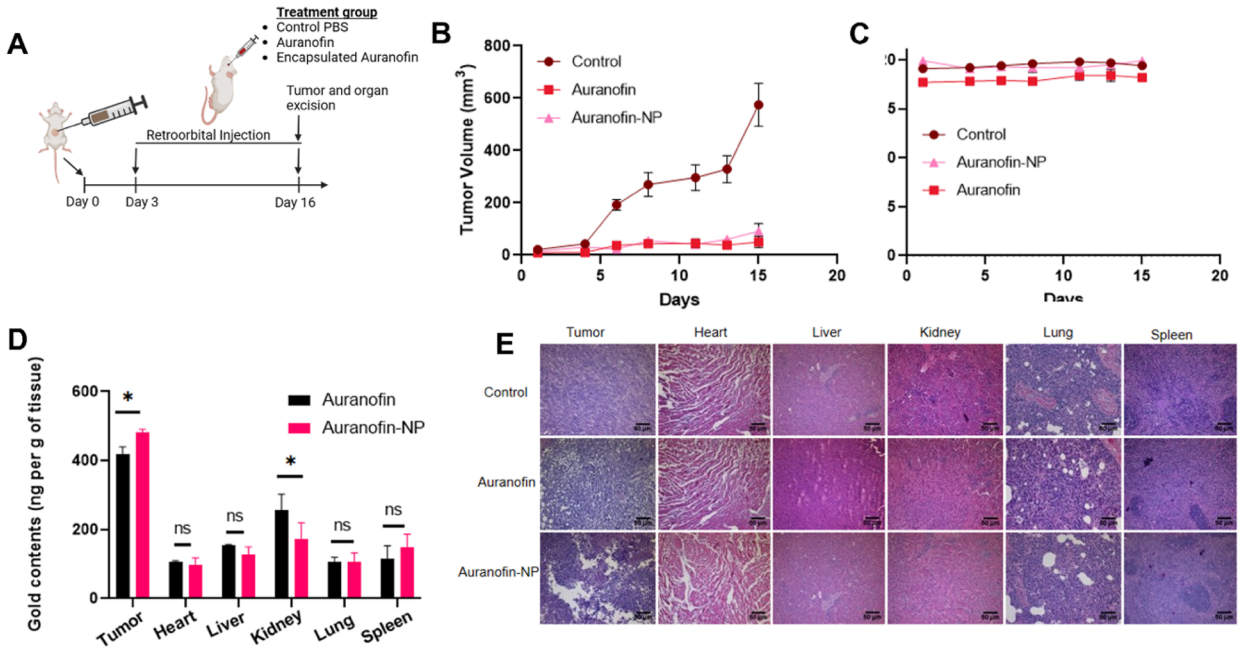

Figure 7. Potency of auranofin and auranofin-NP against MDA-MB-231 xenografts. (A) Six week old female BALB/cJ 4T1 mice were treated via retroorbital injection with phosphate-buffered saline (vehicle control), 5 mg/kg of auranofin, and 3 mg/kg of auranofin nanoparticle (auranofin-NP). (B) Mice from each group (five mice per group) and tumor sizes were measured three times per week for a total of 2 weeks with the mean ± SEM presented. Statistical significance demonstrating the differences in the vehicle control vs auranofin and auranofin-NP was determined using one-way ANOVA with a p value < 0.001, and no significant difference between the auranofin mice group and auranofin-NP group was seen by the t test. (C) Mice from each group were weighed right after injection, and mean ± SEM values are reported. Statistical difference was seen between groups of control and auranofin-NP vs auranofin using one-way ANOVA with a p value < 0.0001. (D) Biodistribution studies using GF-AAS. The organs from various treatment groups (n = 3) were digested using HNO_3 to determine the distribution of gold contents. More accumulation of the gold was seen in the tumor excised from the group treated with auranofin-NP relative to the auranofin group. Gold accumulation was also seen in the kidney of the auranofin mice group compared to nanoparticle groups. (E) Hematoxylin and eosin (H &E) staining on excised organs. Tumor tissues were characterized by disorganized, irregularly shaped cells having hyperchromatic nuclei and abundant stroma. Mild necrosis was present in control. Areas of moderate tumor necrosis and mild acute inflammation were seen in the auranofin treated group, whereas massive and severe necrosis of tumor tissue with some areas of acute inflammation cell was observed in the auranofin-NP group. No abnormal findings were seen in the organs for all groups.

the potential of reduced gold-associated nephrotoxicity with auranofin-NP compared to free auranofin.

To investigate toxicity, we employed histological studies via hematoxylin and eosin (H&E) staining in respective tissues (heart, liver, kidney, lungs, spleen, and tumor) excised at the end of the study in Figure 7E. An independent histopathology scoring performed in a blinded fashion revealed that tumor tissue was characterized by disorganized, irregularly shaped cells having hyperchromatic nuclei and abundant stroma. In some cases, neoplastic cells were present as islands of cells within the stromal connective tissue. Lung tissue was largely consolidated in most samples, likely due to the preparation technique. Kidneys showed some mild postmortem change, primarily the accumulation of proteinaceous material within tubules. Tissues graded as normal typically had these changes, which were not interpreted to be related to the presence of tumor or the experimental treatment. For control mice, metastatic tumor foci were noted in two lung samples. These were present as small foci of tumor cells with scant connective stromal tissue. The treated mice (both auranofin and encapsulated auranofin) had no abnormal findings in the lung, suggestive of no observable toxicity or inhibition of metastasis. The spleen, heart, and liver had no abnormal findings, but extramedullary hematopoiesis was noted in most samples of the liver in all groups.

Strikingly, mice treated with auranofin-loaded NPs showed massive, severe necrosis of tumor tissue and some areas with acute inflammation (infiltration of polymorphonuclear cells) as seen in Figure 8A. Scant healthy tumor tissue remains. Vacuolized tumor cells were present, and large areas were present where strands of tumor stroma had separated where

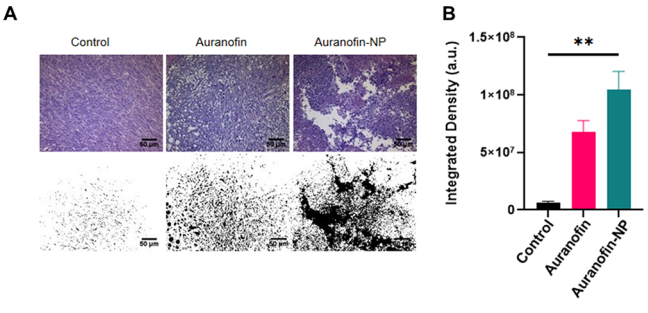

Figure 8. Quantification of necrotic areas of tumors excised from control, auranofin, and auranofin-NP groups using the ImageJ software. Black = necrotic area, white = non-necrotic area (A) Qualitative measurement of necrotic region intensity using the ImageJ software between the control, auranofin, and auranofin-NP groups. Scale bar = 50 μm. (B) Quantification of the tumor necrotic region using the ImageJ software. All p values were calculated using one-way ANOVA with a value <0.0001 between all groups.

https://doi.org/10.1021/acsabm.4c00184
ACS Appl. Bio Mater. 2024, 7, 2012−2022

cancer cells no longer remained. In comparison, auranofin-treated mice had moderate tumor necrosis, and control mice had healthy tumor mass as described earlier. Tumor necrosis between each group (n = 5) was quantified using ImageJ to determine the intensity of the necrotic region (black) vs non-necrotic region (white) as shown in Figure 8B.

Further optimization of the dosing schedule of encapsulated auranofin will likely improve its efficacy toward TNBC based on the relatively low dose treatments with consistent body weight and reduction in possible off-target effects applied in this study. Overall, this points to a drastic effect of auranofin-NP with massive necrotic cell death following treatment compared to free auranofin.

CONCLUSIONS

The combination of a synthetic polymer (PEG) with a natural polymer (chitosan) resulted in a noticeable improvement in solubility compared to that of the natural polymer alone. The composition of formaldehyde plays a role in the recruitment of the PEG on the chitosan, which in turn affects the mechanical properties of chitosan copolymer nanoparticles. The nanoparticle was synthesized using ionic gelation method and showed good release kinetics and efficacy of the drug. Additionally, Chitosan-*g*-PEG nanoparticles synthesized under optimal conditions when employed as a carrier for the drug auranofin have the potential to increase effectiveness against triple-negative breast cancer cells. In vivo results demonstrate that auranofin when delivered with a carrier, in this case, chitosan nanoparticles, shows potency and greater potential for tumor lethality following further optimization procedures of the encapsulated auranofin including dosing.

In summary, this study has demonstrated how changes to surface coating affect stiffness differences and how chitosan-derived nanodelivery of auranofin exhibits effects greater than those of the free drug alone.

ASSOCIATED CONTENT

Supporting Information

The Supporting Information is available free of charge at https://pubs.acs.org/doi/10.1021/acsabm.4c00184.

> Additional information on the biological experiments; NMR of the copolymers and other characterization (Figures S1−S4); nanoparticle characterization including AFM (Figures S5−S14); stability test of nanoparticles (Figure S15); zeta potential of nanoparticles (Figure S16); and apoptosis (Figure S17) (PDF)

AUTHOR INFORMATION

Corresponding Author

Samuel G. Awuah − *Department of Chemistry, University of Kentucky, Lexington, Kentucky 40506, United States; Department of Pharmaceutical Sciences, College of Pharmacy, University of Kentucky, Lexington, Kentucky 40536, United States; University of Kentucky Markey NCI Comprehensive Cancer Center, Lexington, Kentucky 40536, United States; University of Kentucky Bioelectronics and Nanomedicine Research Center, Lexington, Kentucky 40506, United States;* orcid.org/0000-0003-4947-7283; Email: awuah@uky.edu

Authors

Maame Abena O. Afrifa − *Department of Biomedical Engineering, University of Kentucky, Lexington, Kentucky 40506, United States*

Jong H. Kim − *Department of Chemistry, University of Kentucky, Lexington, Kentucky 40506, United States*

Kathryn A. Pitton − *Department of Chemistry, University of Kentucky, Lexington, Kentucky 40506, United States*

Chibuzor Olelewe − *Department of Chemistry, University of Kentucky, Lexington, Kentucky 40506, United States*

Adedamola S. Arojojoye − *Department of Chemistry, University of Kentucky, Lexington, Kentucky 40506, United States*

Douglas R. Strachan − *Department of Astronomy and Physics, University of Kentucky, Lexington, Kentucky 40506, United States;* orcid.org/0000-0002-4172-8204

Mark A. Suckow − *Department of Biomedical Engineering and Department of Biomedical Engineering, University of Kentucky, Lexington, Kentucky 40506, United States*

Complete contact information is available at: https://pubs.acs.org/10.1021/acsabm.4c00184

Author Contributions

Conceptualization: M.A.O.A., S.G.A. Methodology: M.A.O.A., S.G.A. Polymer synthesis and characterization: M.A.O.A., A.S.A. Nanoparticle synthesis and characterization: M.A.O.A. Atomic force microscopy: M.A.O.A., K.A.P., D.R.S. In vitro studies: M.A.O.A. In vivo studies: M.A.O.A., J.H.K., C.O. H & E analysis and interpretation: M.A.O.A., M.A.S. Writing original draft preparation: M.A.O.A. and S.G.A. Writing, review and editing: M.A.O.A. and S.G.A. Supervision: S.G.A. Funding acquisition: S.G.A.

Funding

This work was supported by grant R01CA258421−01 (S.G.A.) from the National Cancer Institute (NCI). The authors also acknowledge support of the Center for Pharmaceutical Research and Innovation (NIH P20GM130456) and UK Research Leadership Academy (RLA), Emerging Themes for Research Program.

Notes

The authors declare the following competing financial interest(s): S.G.A. has patents pending to University of Kentucky Research Foundation. S.G.A. serves on the advisory board and is Chief Science Officer for Phronesis AI.

ACKNOWLEDGMENTS

The following research centers and facilities at the University of Kentucky aided in completing the studies described in this publication. The UK NMR Center supported by NSF (CHE-997738). We would like to thank Dibakar Bhattacharyya, PhD, for laboratory access to the dynamic light scattering (DLS) instrumentation. We thank Dr. Gosia Chwatko for use of her size exclusion chromatography (SEC) and helpful discussions. For the transmission electron microscopy (TEM) characterization, assistance was provided by the Electron Microscopy Center at the University of Kentucky, a member of the KY INBRE (Kentucky IDeA Networks of Biomedical Research Excellence), which is funded by the National Institutes of Health (NIH) National Institute of General Medical Science (IDeA Grant P20GM103436). We would also like to acknowledge BioRender.com for the TOC image.

REFERENCES

(1) Sun, L.; Liu, H.; Ye, Y.; Lei, Y.; Islam, R.; Tan, S.; Tong, R.; Miao, Y.-B.; Cai, L. Smart nanoparticles for cancer therapy. *Signal Transduct Target Ther.* **2023**, *8*, 418.

(2) Goldberg, M.; Manzi, A.; Birdi, A.; Laporte, B.; Conway, P.; Cantin, S.; Mishra, V.; Singh, A.; Pearson, A. T.; Goldberg, E. R.; Goldberger, S.; Flaum, B.; Hasina, R.; London, N. R.; Gallia, G. L.; Bettegowda, C.; Young, S.; Sandulache, V.; Melville, J.; Shun, J.; O'Neill, S. E.; Aydin, E.; Zhavoronkov, A.; Vidal, A.; Soto, A.; Alonso, M. J.; Rosenberg, A. J.; Lingen, M. W.; D'Cruz, A.; Agrawal, N.; Izumchenko, E. A nanoengineered topical transmucosal cisplatin delivery system induces anti-tumor response in animal models and patients with oral cancer. *Nat. Commun.* **2022**, *13*, 4829.

(3) Chehelgerdi, M.; Chehelgerdi, M.; Allela, O. Q. B.; Pecho, R. D. C.; Jayasankar, N.; Rao, D. P.; Thamaraikani, T.; Vasanthan, M.; Viktor, P.; Lakshmaiya, N.; Saadh, M. J.; Amajd, A.; Abo-Zaid, M. A.; Castillo-Acobo, R. Y.; Ismail, A. H.; Amin, A. H.; Akhavan-Sigari, R. Progressing nanotechnology to improve targeted cancer treatment: overcoming hurdles in its clinical implementation. *Mol. Cancer* **2023**, *22*, 169.

(4) Sultan, M. H.; Moni, S. S.; Alqahtani, S. S.; Ali Bakkari, M.; Alshammari, A.; Almoshari, Y.; Alshahrani, S.; Madkhali, O. A.; Mohan, S. Design, physicochemical characterisation, and in vitro cytotoxicity of cisplatin-loaded PEGylated chitosan injectable nano/sub-micron crystals. *Saudi Pharm. J.* **2023**, *31*, 861−873.

(5) Moquin, A.; Hanna, R.; Liang, T.; Erguven, H.; Gran, E. R.; Arndtsen, B. A.; Maysinger, D.; Kakkar, A. PEG-conjugated pyrrole-based polymers: one-pot multicomponent synthesis and self-assembly into soft nanoparticles for drug delivery. *Chem. comm* **2019**, *55*, 9829−9832.

(6) Begines, B.; Ortiz, T.; Pérez-Aranda, M.; Martínez, G.; Merinero, M.; Argüelles-Arias, F.; Alcudia, A. Polymeric nanoparticles for drug delivery: Recent developments and future prospects. *J. Nanomater.* **2020**, *10*, 1403.

(7) Patel, T.; Zhou, J.; Piepmeier, J. M.; Saltzman, W. M. Polymeric nanoparticles for drug delivery to the central nervous system. *Adv. Drug Delivery Rev.* **2012**, *64*, 701−705.

(8) Kumari, A.; Yadav, S. K.; Yadav, S. C. Biodegradable polymeric nanoparticles based drug delivery systems. *Colloids Surf., B* **2010**, *75*, 1−18.

(9) Jawahar, N.; Meyyanathan, S. Polymeric nanoparticles for drug delivery and targeting: A comprehensive review. *Int. j. health allied sci.* **2012**, *1*, 217.

(10) Díez-Martínez, R.; García-Fernández, E.; Manzano, M.; Martínez, Á.; Domenech, M.; Vallet-Regí, M.; García, P. Auranofin-loaded nanoparticles as a new therapeutic tool to fight streptococcal infections. *Sci. Rep.* **2016**, *6*, 19525.

(11) Aibani, N.; Rai, R.; Patel, P.; Cuddihy, G.; Wasan, E. K. Chitosan nanoparticles at the biological interface: Implications for drug delivery. *Pharm.* **2021**, *13*, 1686.

(12) Calvo, P.; Remunan-Lopez, C.; Vila-Jato, J. L.; Alonso, M. J. Novel hydrophilic chitosan-polyethylene oxide nanoparticles as protein carriers. *J. Appl. Polym. Sci.* **1997**, *63*, 125−132.

(13) Calvo, P.; Vila-Jato, J. L.; Alonso, M. a. J. Evaluation of cationic polymer-coated nanocapsules as ocular drug carriers. *Int. J. Pharm.* **1997**, *153*, 41−50.

(14) Berthold, A.; Cremer, K.; Kreuter, J. Preparation and characterization of chitosan microspheres as drug carrier for prednisolone sodium phosphate as model for anti-inflammatory drugs. *J. Controlled Release* **1996**, *39*, 17−25.

(15) Ojeda-Hernández, D. D.; Canales-Aguirre, A. A.; Matias-Guiu, J.; Gomez-Pinedo, U.; Mateos-Díaz, J. C. Potential of chitosan and its derivatives for biomedical applications in the central nervous system. *Front. bioeng. biotechnol.* **2020**, *8*, 389.

(16) Bugamelli, F.; Raggi, M. A.; Orienti, I.; Zecchi, V. Controlled insulin release from chitosan microparticles. *Arch. Pharm.: Int. J. Pharm. Med Chem.* **1998**, *331*, 133−138.

(17) Essa, D.; Choonara, Y. E.; Kondiah, P. P.; Pillay, V. Comparative nanofabrication of PLGA-chitosan-PEG systems employing microfluidics and emulsification solvent evaporation techniques. *Polymer* **2020**, *12*, 1882.

(18) Wang, W.; Meng, Q.; Li, Q.; Liu, J.; Zhou, M.; Jin, Z.; Zhao, K. Chitosan derivatives and their application in biomedicine. *Int. J. Mol. Sci.* **2020**, *21*, 487.

(19) Jiang, L. Q.; Wang, T. Y.; Webster, T. J.; Duan, H.-J.; Qiu, J. Y.; Zhao, Z. M.; Yin, X. X.; Zheng, C. L. Intracellular disposition of chitosan nanoparticles in macrophages: intracellular uptake, exocytosis, and intercellular transport. *Int. J. Nanomedicine* **2017**, *12*, 6383.

(20) Pilipenko, I.; Korzhikov-Vlakh, V.; Sharoyko, V.; Zhang, N.; Schäfer-Korting, M.; Rühl, E.; Zoschke, C.; Tennikova, T. pH-sensitive chitosan−heparin nanoparticles for effective delivery of genetic drugs into epithelial cells. *Pharm.* **2019**, *11*, 317.

(21) Zhang, X.; Zhang, H.; Wu, Z.; Wang, Z.; Niu, H.; Li, C. Nasal absorption enhancement of insulin using PEG-grafted chitosan nanoparticles. *Eur. J. Pharm. Biopharm.* **2008**, *68*, 526−534.

(22) Casettari, L.; Vllasaliu, D.; Castagnino, E.; Stolnik, S.; Howdle, S.; Illum, L. PEGylated chitosan derivatives: Synthesis, characterizations and pharmaceutical applications. *Prog. Polym. Sci.* **2012**, *37*, 659−685.

(23) Vijayan, A.; A, S.; Kumar, G. S. V. PEG grafted chitosan scaffold for dual growth factor delivery for enhanced wound healing. *Sci. Rep.* **2019**, *9*, 1−12.

(24) Sanchez-Salvador, J. L.; Balea, A.; Monte, M. C.; Negro, C.; Blanco, A. Chitosan grafted/cross-linked with biodegradable polymers: A review. *Int. J. Biol. Macromol.* **2021**, *178*, 325−343.

(25) Baharifar, H.; Khoobi, M.; Arbabi Bidgoli, S.; Amani, A. Preparation of PEG-grafted chitosan/streptokinase nanoparticles to improve biological half-life and reduce immunogenicity of the enzyme. *Int. J. Biol. Macromol.* **2020**, *143*, 181−189.

(26) Mjos, K. D.; Orvig, C. Metallodrugs in medicinal inorganic chemistry. *Chem. Rev.* **2014**, *114*, 4540−4563.

(27) McWhinney, S. R.; Goldberg, R. M.; McLeod, H. L. Platinum neurotoxicity pharmacogenetics. *Mol. Cancer Ther.* **2009**, *8*, 10−16.

(28) Rottenberg, S.; Disler, C.; Perego, P. The rediscovery of platinum-based cancer therapy. *Nat. Rev. Cancer* **2021**, *21*, 37−50.

(29) Mertens, R. T.; Gukathasan, S.; Arojojoye, A. S.; Olelewe, C.; Awuah, S. G. Next Generation Gold Drugs and Probes: Chemistry and Biomedical Applications. *Chem. Rev.* **2023**, *123*, 6612−6667.

(30) Yamashita, M. Auranofin: Past to Present, and repurposing. *Int. Immunopharmacol.* **2021**, *101*, No. 108272.

(31) Hatem, E.; Azzi, S.; El Banna, N.; He, T.; Heneman-Masurel, A.; Vernis, L.; Baïlle, D.; Masson, V.; Dingli, F.; Loew, D.; Azzarone, B.; Eid, P.; Baldacci, G.; Huang, M. E. Auranofin/vitamin C: a novel drug combination targeting triple-negative breast cancer. *JNCI* **2019**, *111*, 597−608.

(32) Chaffman, M.; Brogden, R.; Heel, R.; Speight, T.; Avery, G. Auranofin. *Drugs* **1984**, *27*, 378−424.

(33) Cox, A. R.; Masschelin, P. M.; Saha, P. K.; Felix, J. B.; Sharp, R.; Lian, Z.; Xia, Y.; Chernis, N.; Bader, D. A.; Kim, K. H.; Li, X.; Yoshino, J.; Li, X.; Li, G.; Sun, Z.; Wu, H.; Coarfa, C.; Moore, D. D.; Klein, S.; Sun, K.; Hartig, S. M. The rheumatoid arthritis drug auranofin lowers leptin levels and exerts antidiabetic effects in obese mice. *Cell Metab.* **2022**, *34* (1932−1946), No. e1937.

(34) Yan, W.; Zhong, Y.; Hu, X.; Xu, T.; Zhang, Y.; Kales, S.; Qu, Y.; Talley, D. C.; Baljinnyam, B.; LeClair, C. A.; Simeonov, A.; Polster, B. M.; Huang, R.; Ye, Y.; Rai, G.; Henderson, M. J.; Tao, D.; Fang, S. Auranofin targets UBA1 and enhances UBA1 activity by facilitating ubiquitin trans-thioesterification to E2 ubiquitin-conjugating enzymes. *Nat. Commun.* **2023**, *14*, 4798.

(35) Yeo, C. I.; Ooi, K. K.; Tiekink, E. R. Gold-based medicine: a paradigm shift in anti-cancer therapy? *mol* **2018**, *23*, 1410.

(36) Huang, H.; Liao, Y.; Liu, N.; Hua, X.; Cai, J.; Yang, C.; Long, H.; Zhao, C.; Chen, X.; Lan, X.; Zang, D.; Wu, J.; Li, X.; Shi, X.; Wang, X.; Liu, J. Two clinical drugs deubiquitinase inhibitor auranofin and aldehyde dehydrogenase inhibitor disulfiram trigger synergistic anti-tumor effects in vitro and in vivo. *Oncotarget* **2016**, *7*, 2796.

(37) García-Moreno, E.; Tomás, A.; Atrián-Blasco, E.; Gascón, S.; Romanos, E.; Rodriguez-Yoldi, M. J.; Cerrada, E.; Laguna, M. In vitro

https://doi.org/10.1021/acsabm.4c00184
ACS Appl. Bio Mater. 2024, 7, 2012−2022

and in vivo evaluation of organometallic gold (I) derivatives as anticancer agents. *J. Chem. Soc.* **2016**, *45*, 2462−2475.
(38) Lucignano, R.; Pratesi, A.; Imbimbo, P.; Monti, D. M.; Picone, D.; Messori, L.; Ferraro, G.; Merlino, A. Evaluation of Auranofin Loading within Ferritin Nanocages. *Int. J. Mol. Sci.* **2022**, *23*, 14162.
(39) Abdalbari, F. H.; Martinez-Jaramillo, E.; Forgie, B. N.; Tran, E.; Zorychta, E.; Goyeneche, A. A.; Sabri, S.; Telleria, C. M. Auranofin induces lethality driven by reactive oxygen species in high-grade serous ovarian cancer cells. *Cancers* **2023**, *15*, 5136.
(40) Seo, M. J.; Kim, I. Y.; Lee, D. M.; Park, Y. J.; Cho, M. Y.; Jin, H. J.; Choi, K. S. Dual inhibition of thioredoxin reductase and proteasome is required for auranofin-induced paraptosis in breast cancer cells. *Cell Death Dis.* **2023**, *14*, 42.
(41) Garcia, A.; Machado, R. C.; Grazul, R. M.; Lopes, M. T. P.; Corrêa, C. C.; Dos Santos, H. F.; de Almeida, M. V.; Silva, H. Novel antitumor adamantane−azole gold (I) complexes as potential inhibitors of thioredoxin reductase. *J. Biol. Inorg. Chem.* **2016**, *21*, 275−292.
(42) Luo, C.; Wang, P.; He, S.; Zhu, J.; Shi, Y.; Wang, J. Progress and prospect of immunotherapy for triple-negative breast cancer. *Front. Oncol.* **2022**, *12*, No. 919072.
(43) Cortes, J.; Rugo, H. S.; Cescon, D. W.; Im, S. A.; Yusof, M. M.; Gallardo, C.; Lipatov, O.; Barrios, C. H.; Perez-Garcia, J.; Iwata, H.; Masuda, N.; Torregroza Otero, M.; Gokmen, E.; Loi, S.; Guo, Z.; Zhou, X.; Karantza, V.; Pan, W.; Schmid, P. Pembrolizumab plus chemotherapy in advanced triple-negative breast cancer. *N. Engl. J. Med.* **2022**, *387*, 217−226.
(44) Fusco, N.; Sajjadi, E.; Venetis, K.; Ivanova, M.; Andaloro, S.; Guerini-Rocco, E.; Montagna, E.; Caldarella, P.; Veronesi, P.; Colleoni, M.; Viale, G. Low-risk triple-negative breast cancers: Clinico-pathological and molecular features. *Crit. Rev. Oncol. Hematol.* **2022**, No. 103643.
(45) Curigliano, G.; Burstein, H. J.; Winer, E. P.; Gnant, M.; Dubsky, P.; Loibl, S.; Colleoni, M.; Regan, M. M.; Piccart-Gebhart, M.; Senn, H.-J. De-escalating and escalating treatments for early-stage breast cancer: the St. Gallen International Expert Consensus Conference on the Primary Therapy of Early Breast Cancer 2017. *Ann. Oncol.* **2017**, *28*, 1700−1712.
(46) Mittendorf, E. A.; Zhang, H.; Barrios, C. H.; Saji, S.; Jung, K. H.; Hegg, R.; Koehler, A.; Sohn, J.; Iwata, H.; Telli, M. L.; Ferrario, C.; Punie, K.; Penault-Llorca, F.; Patel, S.; Duc, A. N.; Liste-Hermoso, M.; Maiya, V.; Molinero, L.; Chui, S. Y.; Harbeck, N. Neoadjuvant atezolizumab in combination with sequential nab-paclitaxel and anthracycline-based chemotherapy versus placebo and chemotherapy in patients with early-stage triple-negative breast cancer (IMpassion031): a randomised, double-blind, phase 3 trial. *Lancet* **2020**, *396*, 1090−1100.
(47) Derakhshan, F.; Reis-Filho, J. S. Pathogenesis of Triple-Negative Breast Cancer. *Annu. Rev. Pathol.* **2022**, *17*, 181−204.
(48) Ismail-Khan, R.; Bui, M. M. A review of triple-negative breast cancer. *Cancer Control* **2010**, *17*, 173−176.
(49) Miglietta, F.; Dieci, M.; Griguolo, G.; Guarneri, V.; Conte, P. Chemotherapy for advanced HER2-negative breast cancer: Can one algorithm fit all? *Cancer Treat. Rev.* **2017**, *60*, 100−108.
(50) Zhang, Y.; Miyamoto, Y.; Ihara, S.; Yang, J. Z.; Zuill, D. E.; Angsantikul, P.; Zhang, Q.; Gao, W.; Zhang, L.; Eckmann, L. Composite Thermoresponsive Hydrogel with Auranofin-Loaded Nanoparticles for Topical Treatment of Vaginal Trichomonad Infection. *Advanced therapeutics* **2019**, *2*, No. 1900157.
(51) Kupiec, M.; Tomaszewska, A.; Jakubczak, W.; Haczyk-Więcek, M.; Pawlak, K. Speciation Analysis Highlights the Interactions of Auranofin with the Cytoskeleton Proteins of Lung Cancer Cells. *Pharmaceuticals* **2022**, *15*, 1285.
(52) Hui, Y.; Yi, X.; Hou, F.; Wibowo, D.; Zhang, F.; Zhao, D.; Gao, H.; Zhao, C.-X. Role of nanoparticle mechanical properties in cancer drug delivery. *ACS Nano* **2019**, *13*, 7410−7424.
(53) Shimada, Y.; Yamamura, K.; Matsusaka, S. Evaluation of mechanical properties of nanoparticles using a constant-volume shear tester. *Advanced Powder Technology* **2020**, *31*, 1007−1012.
(54) Guo, D.; Xie, G.; Luo, J. Mechanical properties of nanoparticles: basics and applications. *J. Phys. D: Appl. Phys.* **2014**, *47*, No. 013001.
(55) Kulkarni, A. R.; Hukkeri, V. I.; Sung, H. W.; Liang, H. F. A Novel Method for the Synthesis of the PEG-Crosslinked Chitosan with a pH-Independent Swelling Behavior. *Macromol. Biosci.* **2005**, *5*, 925−928.
(56) Chang, F.-C.; Tsao, C.-T.; Lin, A.; Zhang, M.; Levengood, S. L.; Zhang, M. PEG-chitosan hydrogel with tunable stiffness for study of drug response of breast cancer cells. *Polymer* **2016**, *8*, 112.
(57) Kiuchi, H.; Kai, W.; Inoue, Y. Preparation and characterization of poly (ethylene glycol) crosslinked chitosan films. *J. Appl. Polym. Sci.* **2008**, *107*, 3823−3830.
(58) Tanuma, H.; Saito, T.; Nishikawa, K.; Dong, T.; Yazawa, K.; Inoue, Y. Preparation and characterization of PEG-cross-linked chitosan hydrogel films with controllable swelling and enzymatic degradation behavior. *Carbohydr. Polym.* **2010**, *80*, 260−265.
(59) Garaiova, Z.; Strand, S. P.; Reitan, N. K.; Lélu, S.; Størset, S. Ø.; Berg, K.; Malmo, J.; Folasire, O.; Bjørkøy, A.; de L Davies, C. Cellular uptake of DNA−chitosan nanoparticles: The role of clathrin-and caveolae-mediated pathways. *Int. J. Biol. Macromol.* **2012**, *51*, 1043−1051.
(60) Hsu, S.-h.; Ho, T.-T.; Tseng, T.-C. Nanoparticle uptake and gene transfer efficiency for MSCs on chitosan and chitosan-hyaluronan substrates. *Biomater* **2012**, *33*, 3639−3650.
(61) Marzano, C.; Gandin, V.; Folda, A.; Scutari, G.; Bindoli, A.; Rigobello, M. P. Inhibition of thioredoxin reductase by auranofin induces apoptosis in cisplatin-resistant human ovarian cancer cells. *Free Radic. Biol. Med.* **2007**, *42*, 872−881.

https://doi.org/10.1021/acsabm.4c00184
ACS Appl. Bio Mater. 2024, 7, 2012−2022